Electronic Supplementary Material (ESI) for Inorganic Chemistry Frontiers.

Supporting Information

Oxygen vacancy meets partial S substitution: an effective strategy to achieve obvious synergistic effect and adjustable electrochemical behavior in NiFe-LDH for enhanced OER and capacitive performance

Dong Shi[a], Yajun Ji*[a], Faxue Lu[a], Junnan Yao[a], Shixiong Zhang[a], Pengcheng Zhang[a]

[a] *School of Materials and Chemistry, University of Shanghai for Science and Technology, Jungong Road 334#, 200093 Shanghai, China.* *Corresponding author: E-mail: jiyajun@usst.edu.cn

Fax: +86 21 65667144; Tel: +86 21 65667144

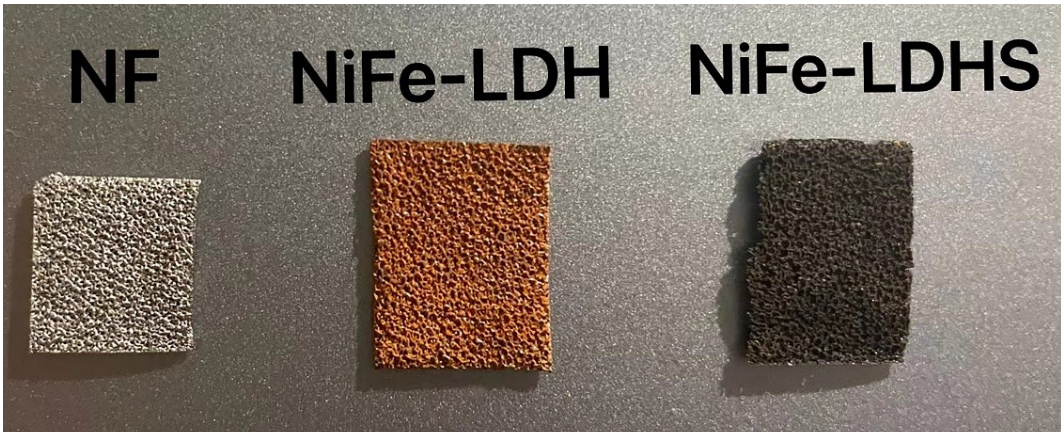

Fig. S1 The Color of bare NFF, NiFe-LDH and NiFe-LDHS.

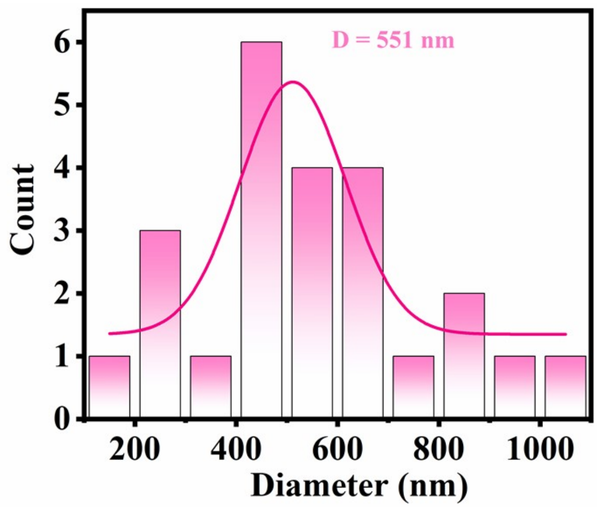

Fig. S2 The pore diameter histogram of the open pore structure.

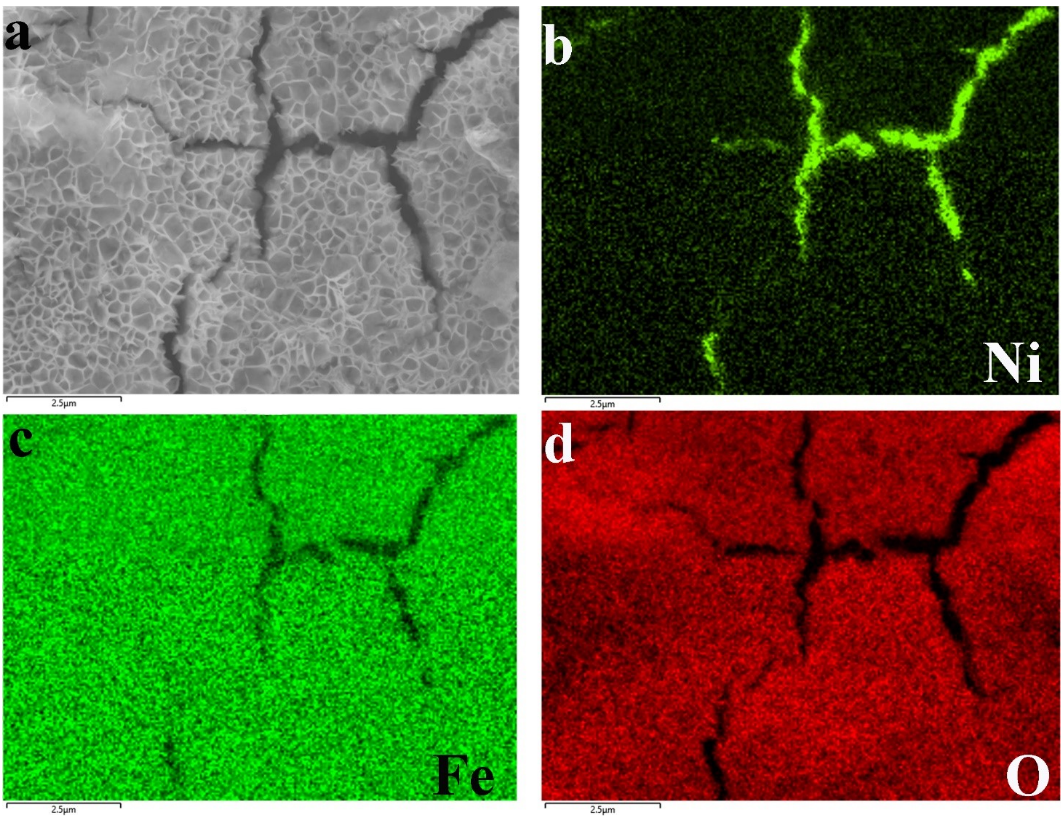

Fig. S3 EDS mapping of NiFe-LDH.

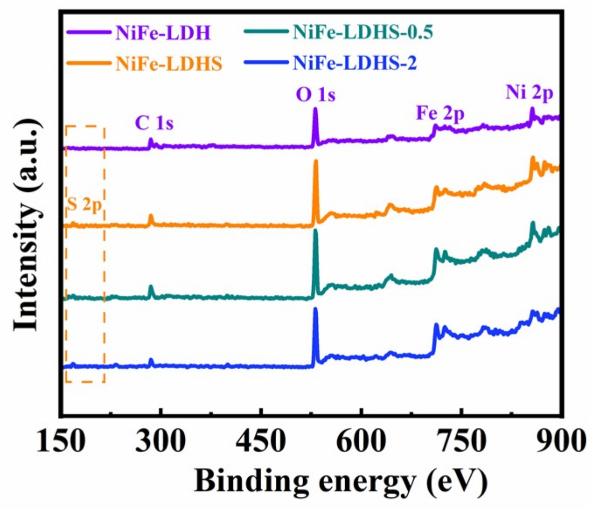

Fig. S4 XPS survey spectra of samples.

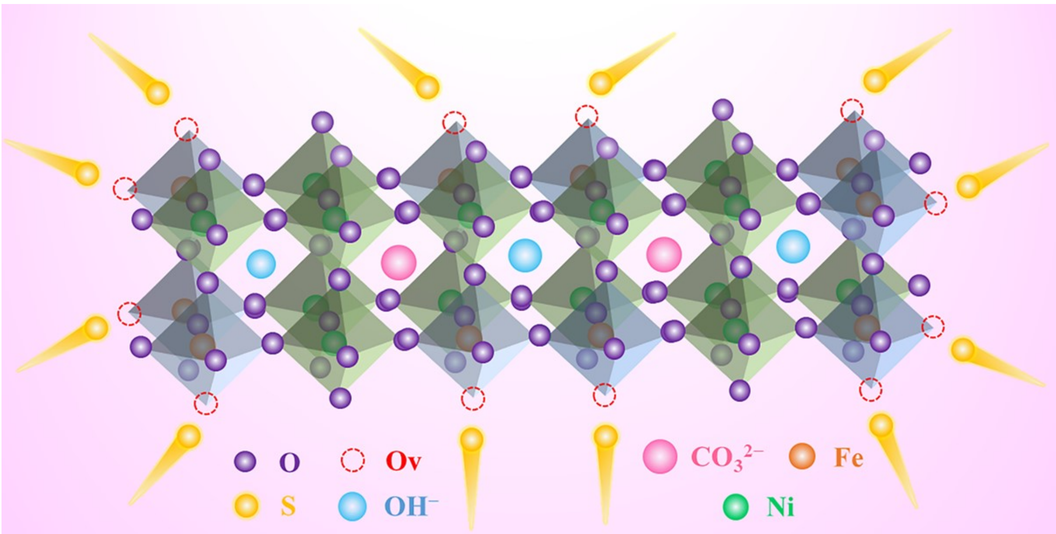

Fig. S5 Schematic diagram of S filling O vacancies in NiFe-LDH. (Notes: Generally, both Ni and Fe show octahedral configuration in NiFe-LDH (MO_6), but Ni presents a more stable configuration. In addition, based on previous report, the content of O_v increases with the elevation of Fe content.[1] Therefore, it can be speculated that O_v usually appeared near the Fe sites (FeO_{6-x}), which provided clues for explaining the appearance of Fe-S bond in the Fe 2p spectrum of NiFe-LDHS.)

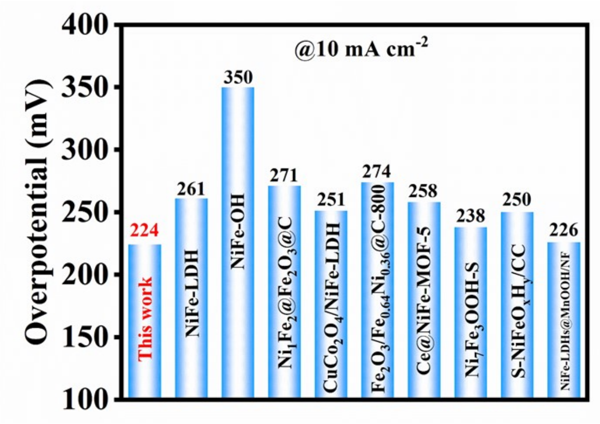

Fig. S6 Comparison of OER performance (mV) for NiFe-LDHS with other Ni/Fe-based electrocatalysts reported in recent years.

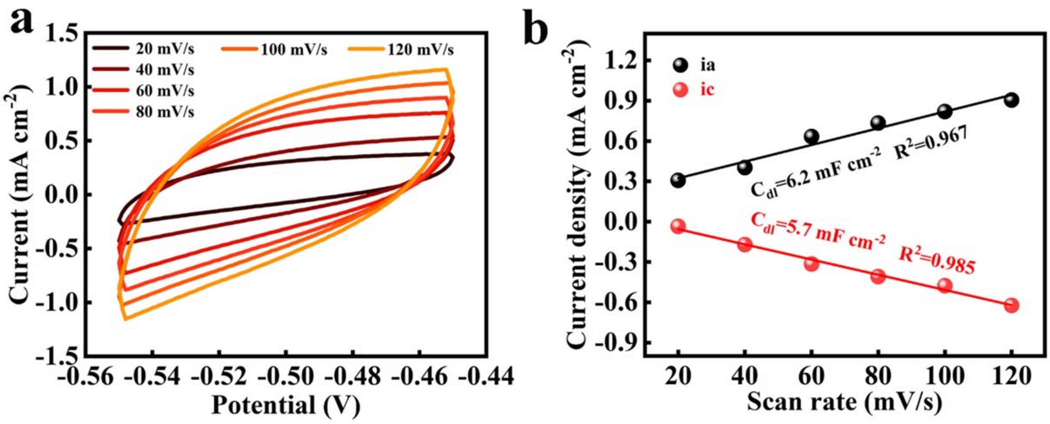

Fig. S7 (a) CV curves of NiFe-LDH at various scan rates. (b) The C_{dl} values of NiFe-LDH.

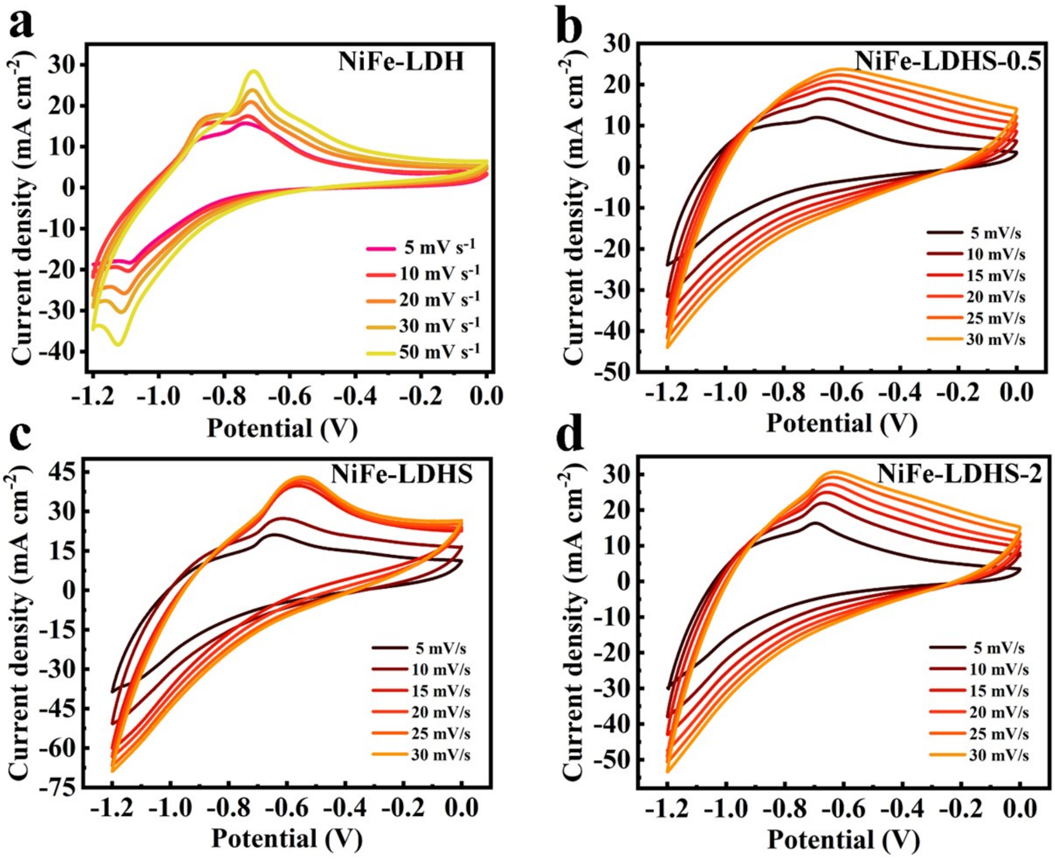

Fig. S8 CV curves of samples at various scan rates.

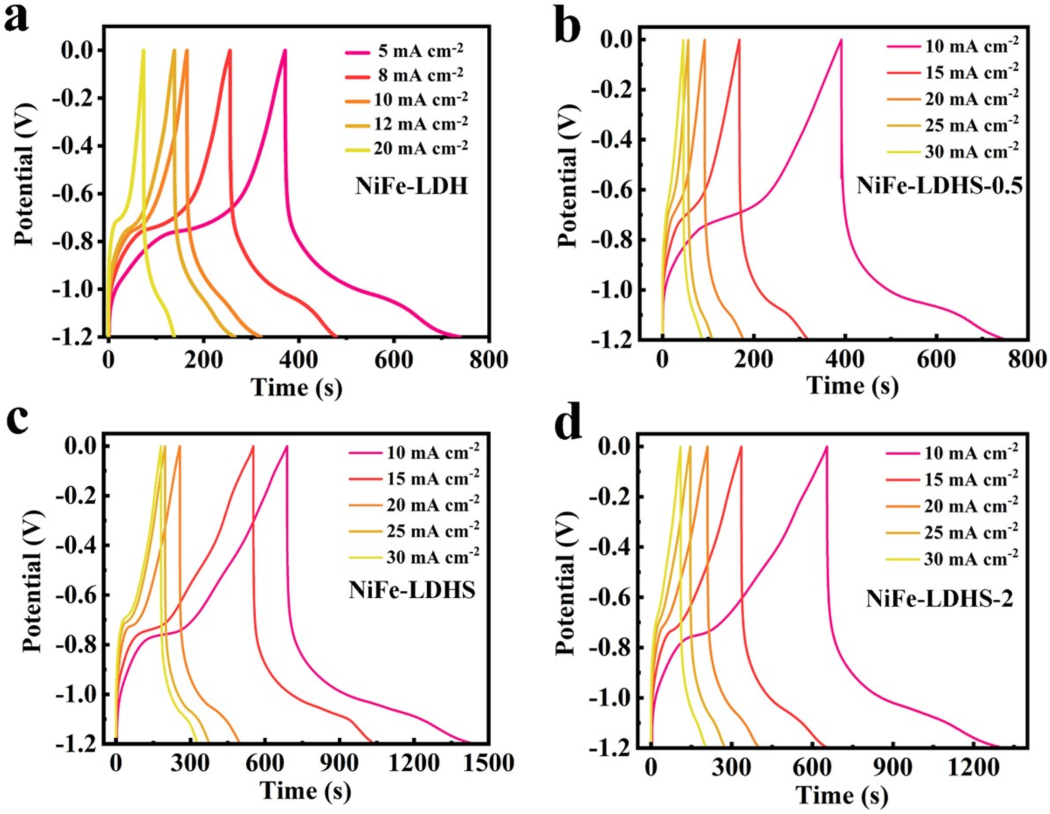

Fig. S9 GCD curves of samples at various current densities.

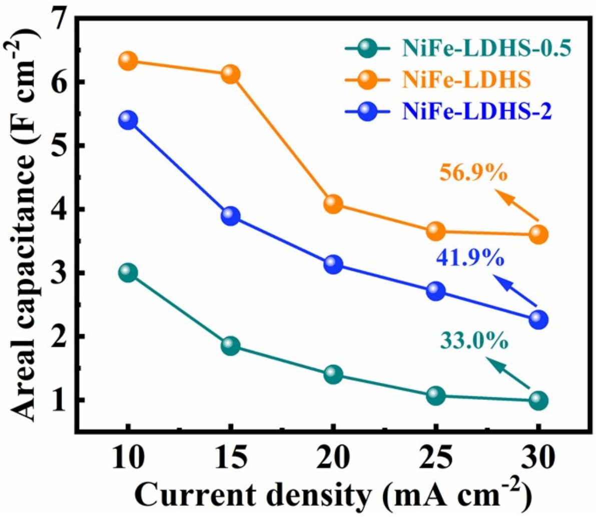

Fig. S10 Rate performance of samples.

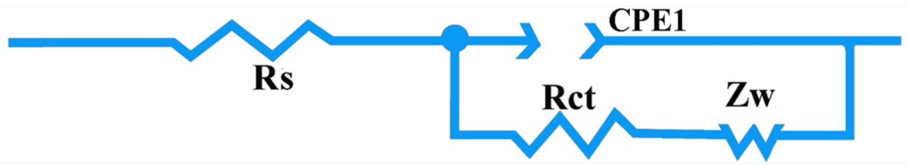

Fig. S11. The corresponding equivalent circuit for fitting the Impedance Nyquist plots.

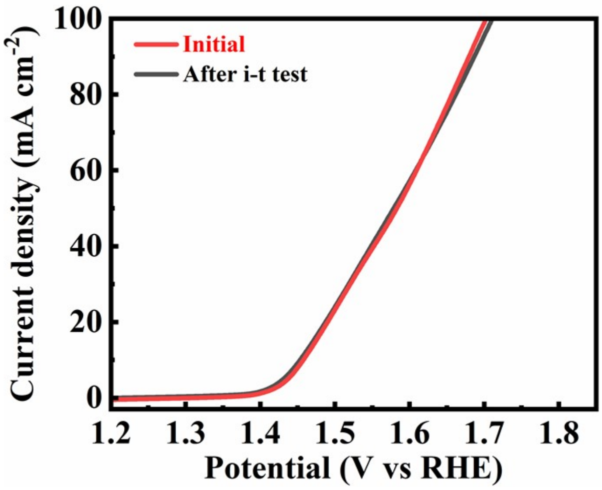

Fig. S12 LSV curves of NiFe-LDHS initial and after 32 h OER.

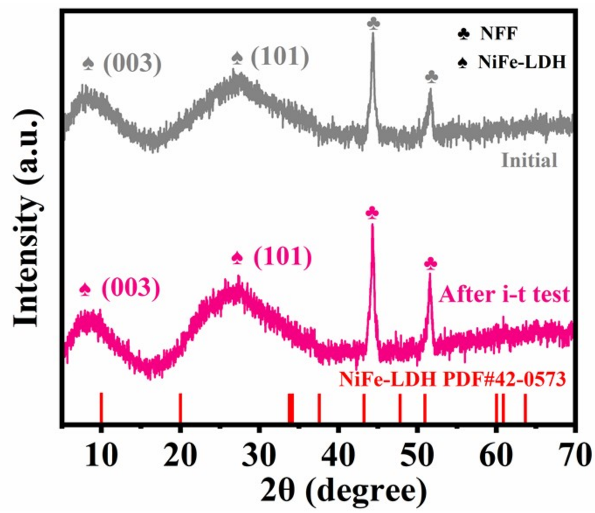

Fig. S13 XRD spectra of NiFe-LDHS initial and after 32 h OER.

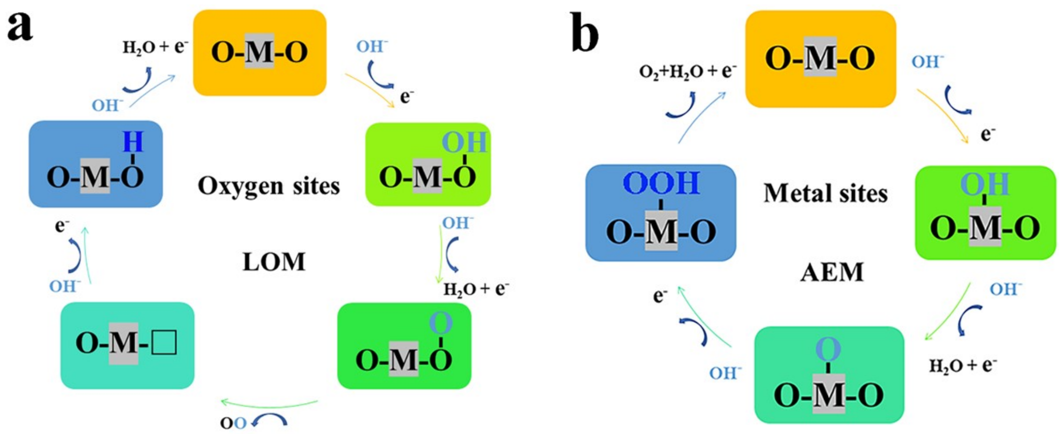

Fig. S14 (a) Lattice-oxygen-mediated mechanism (LOM). (b) Adsorbate evolution mechanism (AEM). (Notes: The LOM and the AEM have different active sites, usually the LOM takes O site as active site and the AEM takes metal site as active site.[1, 2])

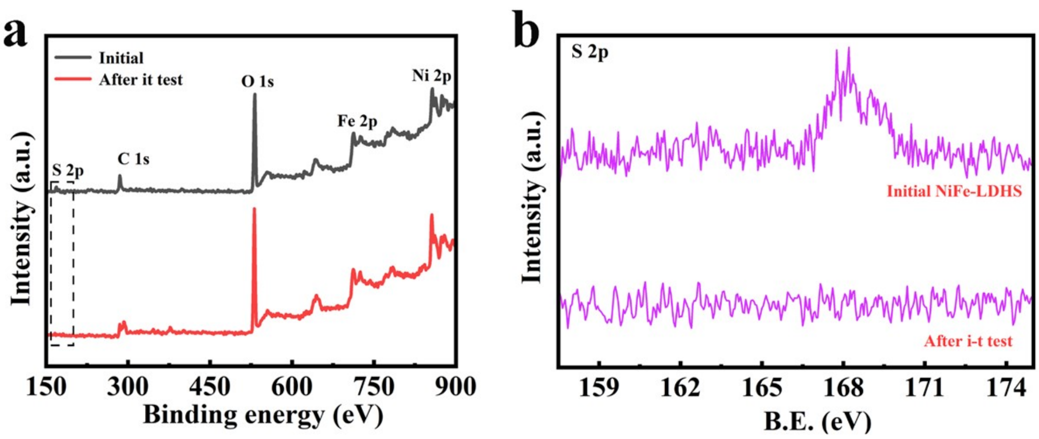

Fig. S15 XPS survey spectra of NiFe-LDHS initial and after 32 h OER.

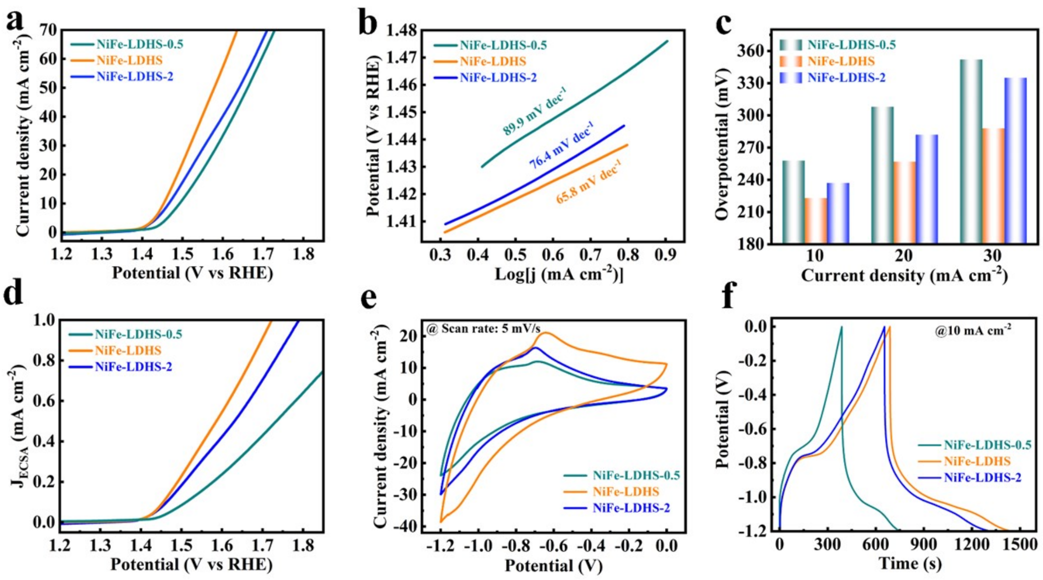

Fig. S16 Comparison of electrochemical properties of electrodes with different sulfidation degrees.

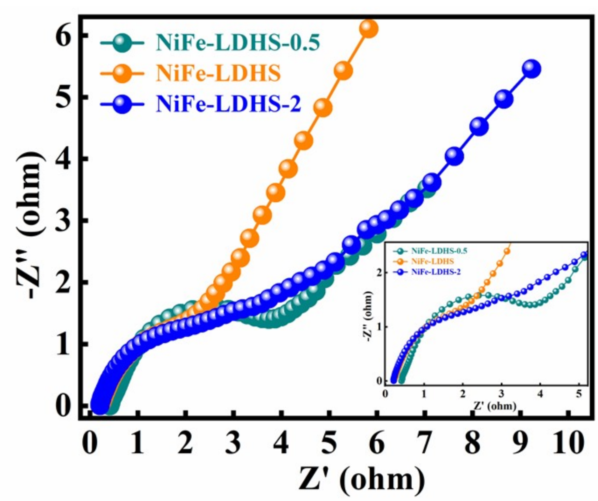

Fig. S17 EIS plots of the samples with different S doping degrees.

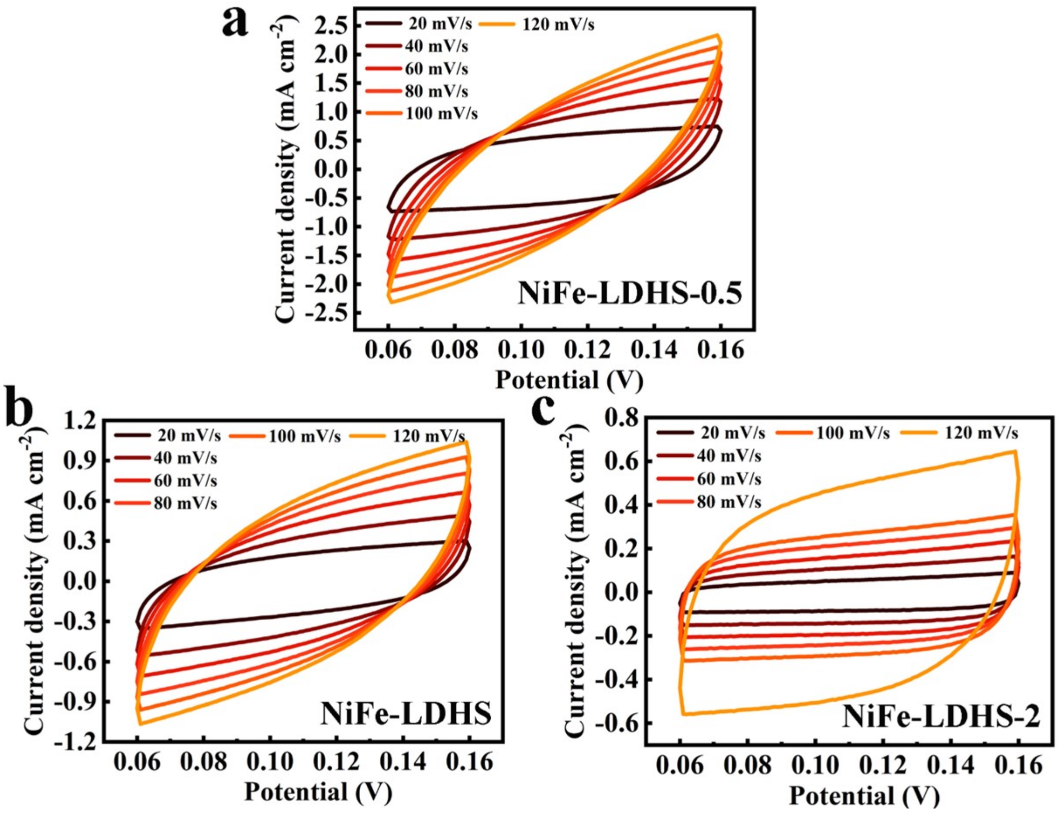

Fig. S18 CV curves of samples with different sulfidation degrees for calculating C_{dl}.

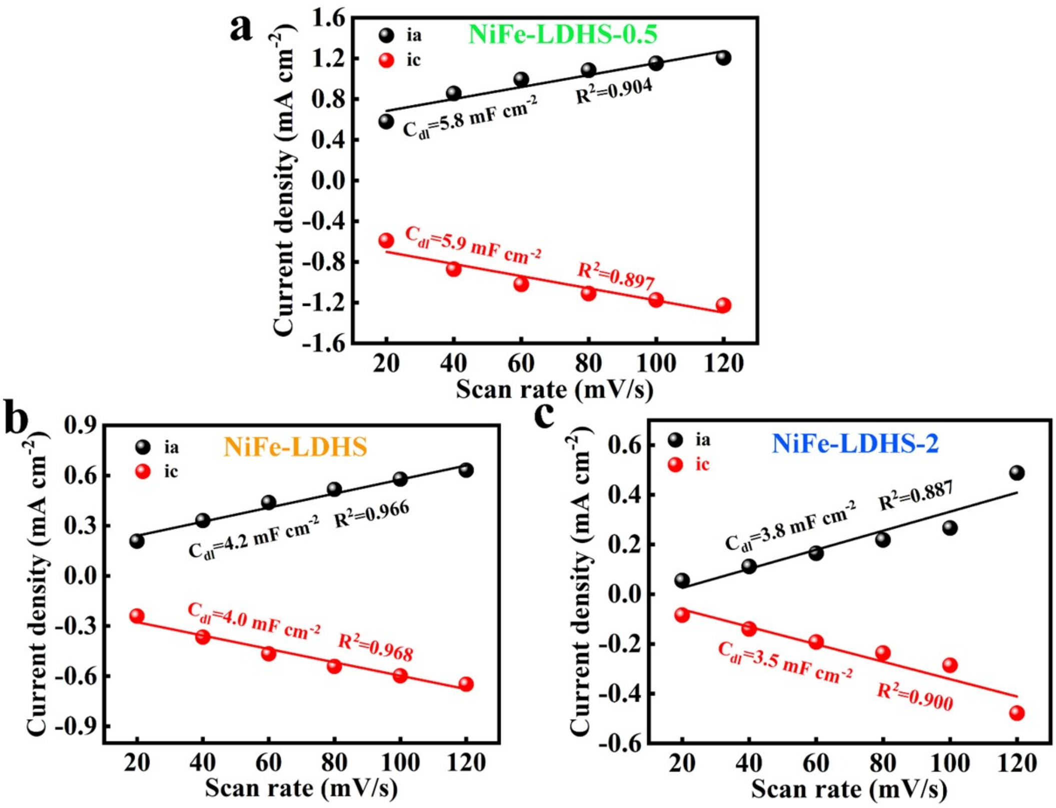

Fig. S19 The C_{dl} values of samples with different sulfidation degrees.

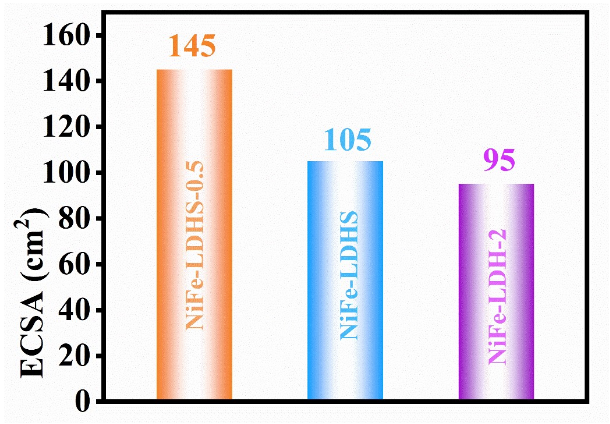

Fig. S20 The values of ECSA of samples with different sulfidation degrees.

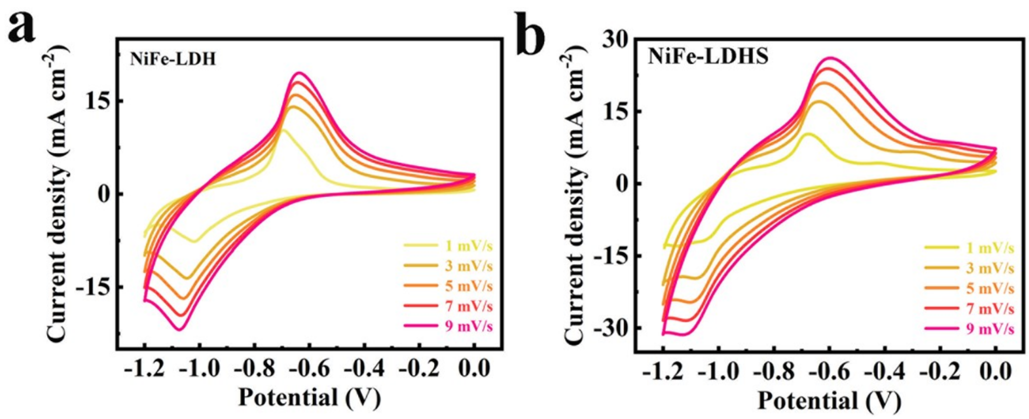

Fig. S21 CV curves of NiFe-LDH and NiFe-LDHS for calculating the b values.

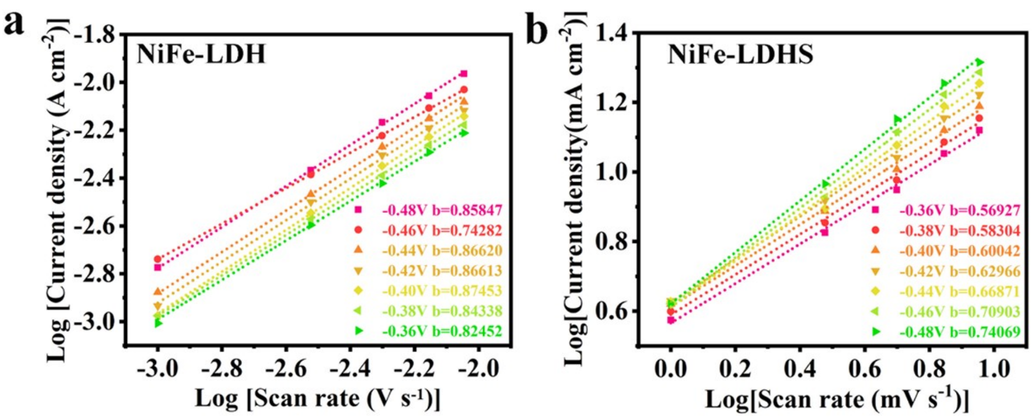

Fig. S22 The b values of NiFe-LDH and NiFe-LDHS at different potentials.

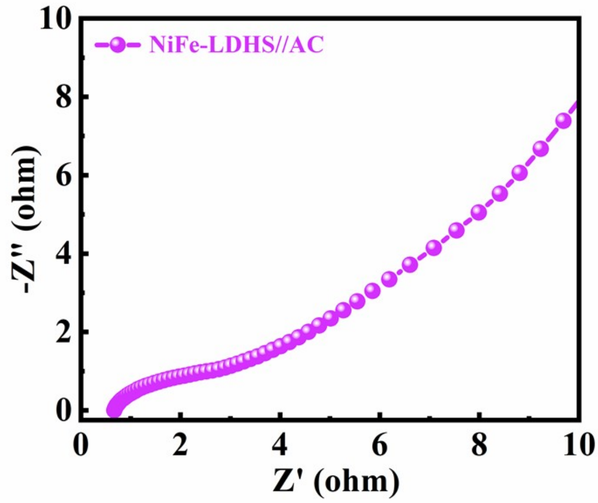

Fig. S23 EIS spectrum of the ASC device.

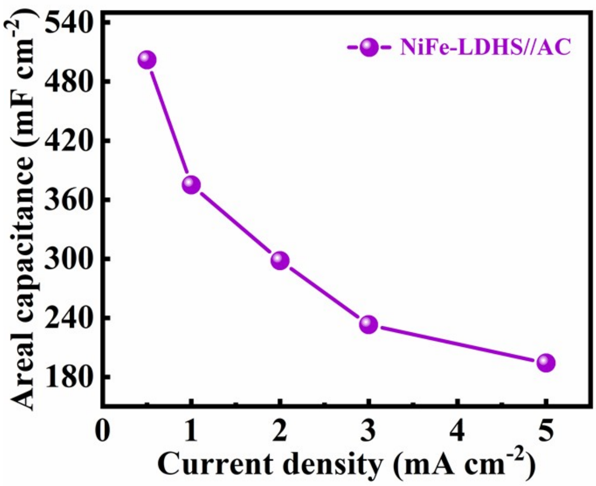

Fig. S24 Areal capacitance of the ASC at different current densities.

Table. S1 Comparison of OER performance (mV) for NiFe-LDHS with other Ni/Fe-based electrocatalysts reported in recent years.

Num	Electrocatalyst	η [mV]	Electrolyte	j (mA cm^{-2})	Refs
1	NiFe-LDHS	224	1 M KOH	10	**This work**
2	NiFe-LDH	261	1 M KOH	10	[3]
3	NiFe-OH	350	0.1 M $KHCO_3$	10	[4]
4	Ni_1Fe_2@Fe_2O_3@C	271	1 M KOH	10	[5]
5	$CuCo_2O_4$/NiFe-LDH	251	1 M KOH	10	[6]
6	Fe_2O_3/$Fe_{0.64}Ni_{0.36}$@C-800	274	1 M KOH	10	[7]
7	Ce@NiFe-MOF-5	258	1 M KOH	10	[8]
8	Ni_7Fe_3OOH-S	238	1 M KOH	10	[9]
9	S-$NiFeO_xH_y$/CC	250	Alkaline Seawater	10	[10]
10	NiFe-LDHs@Gamma-MnOOH/NF	226	1 M KOH	10	[11]

Table. S2 Comparison of the areal specific capacitance between this work and the recent reports on electrode materilas for supercapacitors.

Num	Electrode	C_a (F cm^{-2})	j (mA cm^{-2})	References
1	NiFe-LDHS	**6.33**	10	**This work**
2	$Ti_3C_2T_x$/rGO/Fe_3O_4 (Fe-M/G)	1.25	1	[12]
3	EV-HNSs	0.19	1	[13]
4	3D-CL-A66%	5.25	3	[14]
5	VN/Graphite	0.091	1	[15]
6	Eheat-shaped CuO/MnO_2	0.261	1	[16]
7	$CuFe_2O_4$	2.76	3	[17]
8	$NiCo_2S_4$@W-MX/CF	2.16	3.86	[18]
9	$Ti_3C_2T_X$-Fe_3O_4- CNT	5.52	3	[19]
10	$Ti_3C_2T_x$-MCNT	1.92	3	[20]

Table. S3 Comparison of Rs and Rct for all samples.

Num	Electrocatalyst	Rs (Ω)	Rct (Ω)
1	NiFe-LDH	0.67	3.85
2	NiFe-LDHS-0.5	0.41	3.82
3	NiFe- LDHS	0.22	2.87
4	NiFe- LDHS-2	0.21	2.85

Table. S4 The atom ratios of S in various samples obtained from the integral areas of S peaks in the XPS full spectra.

Sample	Atom (%)
NiFe-LDHS-0.5	4.69
NiFe-LDHS	4.94
NiFe-LDHS-2	6.04

Table. S5 Comparison of the energy density and power density between this work and the recent reports on SCs.

Num	Supercapacitors	E (mWh cm^{-2})	P (mW cm^{-2})	References
1	NiFe-LDHS//AC	**0.28**	**0.5**	**This work**
2	CCTS/NF-3//AC	0.0065	0.14	[21]
3	Gr/ZnO/$Ni(OH)_2$//AC	0.0651	0.75	[22]
4	PPy/MWCNT/c-CVF//PPy/MWCNT/c-CVF	0.155	0.88	[23]
5	$Ni(OH)_2$//FS-V_2O_5/CNTs	0.0254	4.66	[24]
6	CPYF-ZIF-67-PPy//CPYF-ZIF-67-PPy	0.112	0.2	[25]
7	N-PANI//N-PANI	0.065	0.3	[26]
8	GF@PA@PPy-40//GF@PA@PPy-40	0.0732	0.25	[27]
9	N-rGO/NF//$Ni(OH)_2$@CuO@Cu	0.13	1.6	[28]
10	P-CoS_{1-x}/CNT//CoS@PPy/CNT	0.18	0.45	[29]

References

[1] Y. Zhai, X. Ren, Y. Sun, D. Li, B. Wang, S. Liu, Synergistic effect of multiple vacancies to induce lattice oxygen redox in NiFe-layered double hydroxide OER catalysts, Appl. Catal. B. 323 (2023) 122091, https://doi.org/10.1016/j.apcatb.2022.122091.

[2] J. Song, C. Wei, Z. Huang, C. Liu, L. Zeng, X. Wang, Z.J. Xu, A review on fundamentals for designing oxygen evolution electrocatalysts, Chem. Soc. Rev. 49 (2020) 2196-2214, https://doi.org/10.1039/c9cs00607a.

[3] Y. Zheng, H. Deng, H. Feng, G. Luo, R. Tu, L. Zhang, Triethanolamine-assisted synthesis of NiFe layered double hydroxide ultrathin nanosheets for efficient oxygen evolution reaction,

J. Colloid Interface Sci. 629 (2023) 610-619, https://doi.org/10.1016/j.jcis.2022.09.053.

[4] D. Zhong, D. Wang, T. Li, L. Hao, Z. Ma, T. Zhao, G. Hao, X. Wang, G. Liu, J. Li, Q. Zhao, $NiFeO_xH_y$ with electron-deficient Ni^{2+} for oxygen evolution in mild media, J. Power Sources 556 (2023) 232444, https://doi.org/10.1016/j.jpowsour.2022.232444.

[5] Y. Xue, X. Zhang, J. Yao, J. Zhao, Y. Xu, Q. Yan, K. Ye, K. Zhu, D. Cao, G. Wang, Ultrathin Fe_2O_3 shell-encapsulated NiFe alloy nanoparticles embedded in tubular carbon matrix for enhanced oxygen evolution reaction, J. Alloys Compd. 935 (2023) 167922, https://doi.org/10.1016/j.jallcom.2022.167922.

[6] F. Arshad, A. Munir, A. Tahir, S. Z. Hussain, A. Jilani, A. Hussain, N. Ullah, F. Sher, I. Hussain, Microwave-assisted growth of spherical core-shell NiFe LDH@Cu_xO nanostructures for electrocatalytic water oxidation reaction, Int. J. Hydrogen Energy 48 (2023) 4719-4727, https://doi.org/10.1016/j.ijhydene.2022.10.252.

[7] F. Zhou, M. Gan, D. Yan, X. Chen, X. Peng, Hydrogen-Rich pyrolysis from Ni-Fe heterometallic schiff base centrosymmetric cluster facilitates NiFe alloy for efficient OER electrocatalysts, Small (2023) 2208276, https://doi.org/10.1002/smll.202208276.

[8] X. Wei, D. Liu, C. Wang, R. Yu, K. Zhang, S. Li, Z. Wu, Y. Du, Ce-modified flowerlike NiFe-MOF nanostructure based on ion competitive coordination for enhancing the oxygen evolution reaction, Inorg. Chem. 62 (2023) 3238–3247, https://doi.org/10.1021/acs.inorgchem.2c04261.

[9] W. Liu, X. Wang, F. Wang, X. Liu, Y. Zhang, W. Li, Y. Guo, H. Yin, D. Wang, Electrochemical hydroxidation of sulfide for preparing sulfur-doped NiFe (oxy) hydroxide towards efficient oxygen evolution reaction, Chem. Eng. J. 454 (2023) 140030, https://doi.org/10.1016/j.cej.2022.140030.

[10] Y. Zhang, X. Song, S. Xue, Y. Liang, H. Jiang, Fabrication of hierarchically structured S-doped NiFe hydroxide/oxide electrodes for solar-assisted oxygen evolution reaction in seawater splitting, Appl. Catal. A-Gen. 649 (2023) 118965, https://doi.org/10.1016/j.apcata.2022.118965.

[11] S. Wang, Y. Xia, Z. Xin, L. Xu, Fabrication of the novel NiFe-LDHs @gamma-MnOOH nanorod electrocatalyst for effective water oxidation, Catal. Commun. 173 (2023) 106564, https://doi.org/10.1016/j.catcom.2022.106564.

[12] L. Zhang, K. Yu, Y. Li, Z. Wang, K. Zhan, J. Yang, B. Zhao, Nanoparticles of Fe_3O_4 anchored on $Ti_3C_2T_X$ MXene/rGO aerogels as negative electrodes for advanced supercapacitors, ACS Appl. Nano Mater. 6 (2023) 482-491, https://doi.org/10.1021/acsanm.2c04589.

[13] Z. Ding, Z. Cheng, N. Shi, Z. Guo, Y. Ren, M. Han, M. Chen, L. Xie, W. Huang, Dual-electroactive metal-organic framework nanosheets as negative electrode materials for supercapacitors, Chem. Eng. J. 450 (2022) 137193, https://doi.org/10.1016/j.cej.2022.137193.

[14] Y. Katsuyama, N. Haba, H. Kobayashi, K. Iwase, A. Kudo, I. Honma, R. B. Kaner, Macro- and nano-porous 3D-hierarchical carbon lattices for extraordinarily high capacitance supercapacitors, Adv. Funct. Mater. 32 (2022) 2201544, https://doi.org/10.1002/adfm.202201544.

[15] A. Ramadoss, A. Mohanty, K. G. Saravanan, M. Kundu, S. Z. Noby, K. Kirubavathi, K. Selvaraju, L.S. Mende, Construction of light-weight and flexible vanadium nitride coated graphite paper electrodes for supercapacitors, Ionics 28 (2022) 2513-2524, https://doi.org/10.1007/s11581-022-04529-z.

[16] B. Liu, L. Tian, X. Zheng, Z. Xing, MnO_2 films deposited on CuO nanomaterials as electrode materials for supercapacitors, J. Alloys Compd. 911 (2022) 165003, https://doi.org/10.1016/j.jallcom.2022.165003.

[17] W. Liang, W. Yang, S. Sakib, I. Zhitomirsky, Magnetic $CuFe_2O_4$ nanoparticles with pseudocapacitive properties for electrical energy storage, Molecules 27 (2022) 5313, https://doi.org/10.3390/molecules27165313.

[18] D. D. Khumujam, T. Kshetri, T. I. Singh, N. H. Kim, J. H. Lee, Fibrous asymmetric supercapacitor based on wet spun MXene/PAN fiber-derived multichannel porous MXene/CF negatrode and $NiCo_2S_4$ electrodeposited MXene/CF positrode, Chem. Eng. J. 449 (2022) 137732, https://doi.org/10.1016/j.cej.2022.137732.

[19] W. Liang, I. Zhitomirsky, Composite Fe_3O_4-MXene-Carbon nanotube electrodes for supercapacitors prepared using the new colloidal method, Materials 14 (2021) 2930, https://doi.org/10.3390/ma14112930.

[20] W. Liang, I. Zhitomirsky, MXene-carbon nanotube composite electrodes for high active mass asymmetric supercapacitors, J. Mater. Chem. A 9 (2021) 10335-10344,

https://doi.org/10.1039/d0ta12485k.

[21] W. Wu, X. Wang, X. Wang, F. Li, T. Xu, X. Li, Nanoflower-like Cu_2CoSnS_4 grown on nickel foam as binder-free electrode material for asymmetric supercapacitors with high rate and capacitance, J. Alloys Compd. 947 (2023) 169590, https://doi.org/10.1016/j.jallcom.2023.169590.

[22] S. E. Berrabah, A. Benchettara, F. Smaili, A. Benchettara, A. Mahieddine, High performance hybrid supercapacitor based on electrochemical deposed of nickel hydroxide on zinc oxide supported by graphite electrode, J. Alloys Compd. 942 (2023) 169112, https://doi.org/10.1016/j.jallcom.2023.169112.

[23] Q. Zhang, D. Liu, H. Pei, W. Pan, Y. Liu, S. Xu, S. Cao, Swelling-reconstructed chitosan-viscose nonwoven fabric for high-performance quasi-solid-state supercapacitors, J. Colloid Interface Sci. 617 (2022) 489-499, https://doi.org/10.1016/j.jcis.2022.03.011.

[24] C. Shi, J. Sun, Y. Pang, Y. Liu, B. Huang, B. Liu, A new potassium dual-ion hybrid supercapacitor based on battery-type $Ni(OH)_2$ nanotube arrays and pseudocapacitor-type V_2O_5-anchored carbon nanotubes electrodes, J. Colloid Interface Sci. 607 (2022) 462-469, https://doi.org/10.1016/j.jcis.2021.09.011.

[25] Y. Liang, X. Luo, Z. Hu, L. Yang, Y. Zhang, L. Zhu, M. Zhu, Deposition of ZIF-67 and polypyrrole on current collector knitted from carbon nanotube-wrapped polymer yarns as a high-performance electrode for flexible supercapacitors, J. Colloid Interface Sci. 631 (2023) 77-85, https://doi.org/10.1016/j.jcis.2022.10.155.

[26] J. Wang, Y. Ma, J. Liu, L. Zhu, X. Wu, X. Huang, Facile and controllable in-situ nitridation of polyaniline electrode for high-performance flexible all-solid-state supercapacitors, J. Colloid Interface Sci. 620 (2022) 399-406, https://doi.org/10.1016/j.jcis.2022.04.038.

[27] Y. Chen, Z. Yin, D. Huang, L. Lei, S. Chen, M. Yan, L. Du, R. Xiao, M. Cheng, Uniform polypyrrole electrodeposition triggered by phytic acid-guided interface engineering for high energy density flexible supercapacitor, J. Colloid Interface Sci. 611 (2022) 356-365, https://doi.org/10.1016/j.jcis.2021.12.090.

[28] M. Li, A. Addad, P. Roussel, S. Szunerits, R. Boukherroub, High performance flexible hybrid supercapacitors based on nickel hydroxide deposited on copper oxide supported by

copper foam for a sunlight-powered rechargeable energy storage system, J. Colloid Interface Sci. 579 (2020) 520-530, https://doi.org/10.1016/j.jcis.2020.06.092.

[29] Q. Wang, Z. Qu, S. Chen, D. Zhang, Metal organic framework derived P-doping CoS@C with sulfide defect to boost high-performance asymmetric supercapacitors, J. Colloid Interface Sci. 624 (2022) 385-393, https://doi.org/10.1016/j.jcis.2022.03.053.